NANO LETTERS

pubs.acs.org/NanoLett

Letter

30°-Twisted Bilayer Graphene Quasicrystals from Chemical Vapor Deposition

Sergio Pezzini,* Vaidotas Mišeikis, Giulia Piccinini, Stiven Forti, Simona Pace, Rebecca Engelke, Francesco Rossella, Kenji Watanabe, Takashi Taniguchi, Philip Kim, and Camilla Coletti*

Cite This: *Nano Lett.* 2020, 20, 3313−3319

Read Online

ACCESS | Metrics & More | Article Recommendations | Supporting Information

ABSTRACT: The artificial stacking of atomically thin crystals suffers from intrinsic limitations in terms of control and reproducibility of the relative orientation of exfoliated flakes. This drawback is particularly severe when the properties of the system critically depends on the twist angle, as in the case of the dodecagonal quasicrystal formed by two graphene layers rotated by 30°. Here we show that large-area 30°-rotated bilayer graphene can be grown deterministically by chemical vapor deposition on Cu, eliminating the need of artificial assembly. The quasicrystals are easily transferred to arbitrary substrates and integrated in high-quality hexagonal boron nitride-encapsulated heterostructures, which we process into dual-gated devices exhibiting carrier mobility up to 10^5 $cm^2/(V\,s)$. From low-temperature magnetotransport, we find that the graphene quasicrystals effectively behave as uncoupled graphene layers, showing 8-fold degenerate quantum Hall states. This result indicates that the Dirac cones replica detected by previous photoemission experiments do not contribute to the electrical transport.

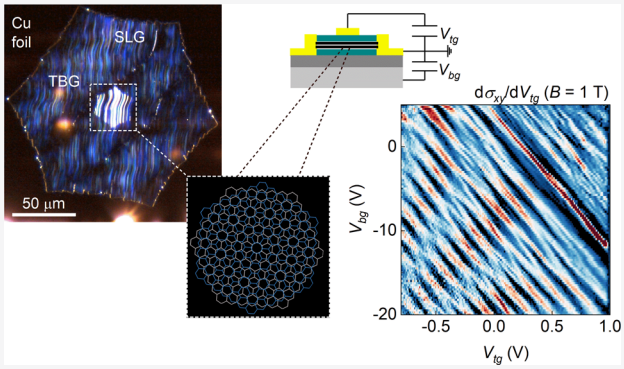

KEYWORDS: *Twisted bilayer graphene, chemical vapor deposition, dodecagonal quasicrystals, quantum Hall effect*

Twisted bilayer graphene (TBG), a system made of two stacked single-layer graphene (SLG) with misaligned crystallographic orientation, is providing an incredibly rich platform for novel physical phenomena.[1,2] In the limit of small twist angle (<10°), the long-range moiré superpotential determines important modifications to the structural and electronic properties.[3−5] For larger twisting, TBG falls in a weak coupling regime, with the electronic properties resembling those of two SLG conducting in parallel.[6,7] However, considerable interlayer coupling seems to re-emerge in TBG with a twist angle of precisely 30°, giving rise to multiple Dirac cones replica, as detected by angle-resolved photoemission spectroscopy (ARPES) in two recent experiments.[8,9] In this configuration, TBG forms an incommensurate structure with 12-fold rotational symmetry, although lacking of translational symmetry, known as dodecagonal quasicrystal (QC). In addition to the cones' multiplication, QC-TBG is predicted to host spiral Fermi surfaces resulting in novel quantum oscillations,[10] van Hove singularities,[11,12] and semilocalized electronic states following the dodecagonal tiling,[11] which strongly motivates further experimental investigation, in particular low-temperature electrical transport in high-mobility devices. However, QC-TBG is extremely sensitive to small variation in the twist angle, which makes it highly challenging to realize it with the common hexagonal boron nitride (hBN)-mediated "tear-and-stack" approach.[13] The samples presented by Anh et al.[8] and Yao et al.[9] were grown on SiC and Pt(111) substrates, respectively, which pose severe limitation to the possibility of transfer and processing high-mobility transport devices. Chemical vapor deposition (CVD) of single-crystalline graphene bilayer on Cu foils offers an appealing alternative approach, as it allows to obtain large-area defect-free samples that can be isolated from the growth catalyst and encapsulated in hBN flakes with several methods.[14,15] Moreover, a few works have suggested the possibility of a highly selective growth mechanism, strongly favoring the AB and 30°-rotated stacking over random twisting on Cu(111) foils[16] and Cu/Ni gradient alloy.[17] We found that our CVD process for isolated graphene single crystals[18,19] yields large-area bilayers with AB or QC-TBG configurations exclusively. The two types can be easily distinguished on the basis of the relative orientations of the hexagonal edges of the two layers, allowing for large-scale production of QC-TBG, transfer to arbitrary substrates and

Received: January 14, 2020
Revised: April 8, 2020
Published: April 16, 2020

https://dx.doi.org/10.1021/acs.nanolett.0c00172
Nano Lett. 2020, 20, 3313−3319

device processing. The QC-TBG configuration is unambiguously identified by transmission electron microscopy (TEM) measurements on suspended samples and supported by Raman spectroscopy. We fabricated hBN-encapsulated dual-gated devices and probed for the first time the low-temperature magnetotransport properties of QC-TBG.

To produce the graphene crystals, we made use of electropolished high-purity Cu foils (~2 cm^2) and performed low-pressure CVD in a commercial cold-wall reactor, limiting the gas flow via a quartz enclosure (more details can be found in SI and refs 18 and 19). We obtained isolated hexagonal graphene domains with 150−250 μm lateral dimensions, with additional hexagonal concentric bilayer regions with 10−50 μm lateral dimensions, sharing the same nucleation center as the monolayer portion (see Figure 1a,b). Dark-field optical imaging on the Cu foil allows easy identification of the graphene flakes and discerning of the stacking order of the bilayer region. Over a representative growth cycle, we observed a total of 114 graphene single crystals with bilayer portions. Among them, 59% showed AB stacking (confirmed by Raman spectroscopy, see Figure S1) and 41% showed 30° rotation; no other stacking was identified by optical inspection. While AB stacking is energetically favored by interlayer van der Waals interaction,[20] and therefore dominates in natural graphite crystals, the incommensurate QC-TBG (Figure 1c) can be stabilized by the surface morphology of the growth substrate. Yan et al.[16] showed that the interaction between step edges on Cu(111) and the graphene layers at the nucleation stage is optimal for straight (zigzag or armchair) graphene edges oriented along the step direction. This preference applies to repeated sequential nucleation in multilayers growth and makes the 0° and 30° twisting (approximately) isoenergetic, favoring them over random angles. In our case, graphene is synthesized over large predominantly (111) domains, obtained with short-time annealing (more details in SI and ref 18), where AB stacked and QC bilayers are equally probable according to ref 16. In this sense, additional control on the stepped surface morphology via fine-tuning of the annealing parameters is not expected to increase significantly the occurrence of QC-TBG with respect to that of AB bilayers. Although additional multilayer patches can attain non-negligible size for longer growth time, they can be easily identified and avoided during further characterization and processing of the QC-TBG. To isolate the CVD-grown QC-TBG from the Cu catalyst, we employed a semidry PMMA-mediated transfer technique, based on electrochemical delamination from Cu[21] and deterministic lamination onto an arbitrary substrate (more details can be found in SI and ref 19). In Figure 1d, we show a typical graphene crystal with 30°-rotated bilayer portion after transfer to SiO_2 (285 nm)/Si, showing no visible wrinkles, cracks, or macroscopic contamination. We then adopted the procedure described in refs 15 and 22 to pick up the QC-TBG from SiO_2 with hBN flakes (10−50 nm thick) and assemble encapsulated structures with large contamination-free areas (see Figure S2 for optical and atomic force microscopy images). Straight edges of the hBN flakes were intentionally misaligned with respect to the two hexagonal layers, ideally falling at 15° misorientation, minimizing the chance of an hBN-induced moiré superstructure. Moreover, despite the fact that high temperatures favor the interface cleaning process,[22] the assembly was performed keeping T < 170 °C to avoid possible motion of the encapsulated graphene sheets[23] and relaxation of the TBG toward AB stack.[24]

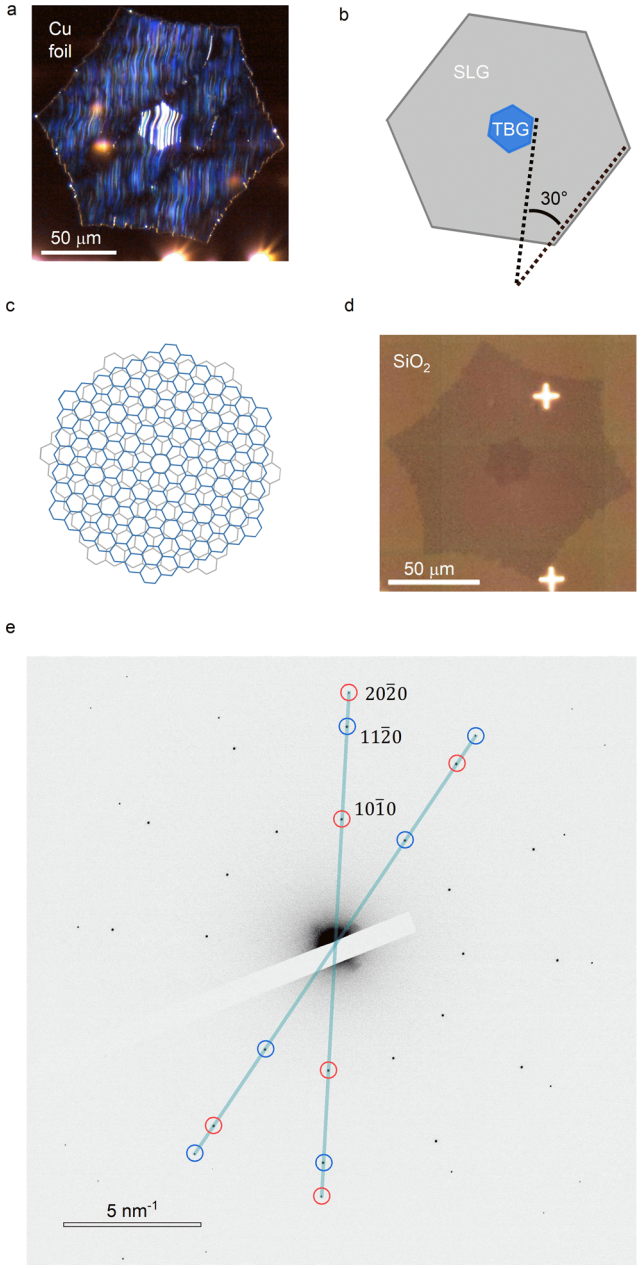

Figure 1. (a) Dark-field optical microscopy image of a typical QC-TBG grown by CVD on Cu foil. (b) Schematic structure of the sample shown in (a), with the two superimposed concentric hexagons rotated by 30°. (c) Sketch of the crystal structure of the 12-fold rotationally symmetric QC-TBG. (d) Bright-field microscopy image of a QC-TBG after transfer by semidry method on a SiO_2 (285 nm)/Si wafer. (e) TEM SAED obtained on a QC-TBG suspended over a TEM grid. The red (blue) circles identify the Bragg peaks from the top (bottom) graphene layers. Three groups of spots are detected and labeled according to their Miller indices. The straight lines are guides to the eye showing the radial alignment of peaks form different layers.

In Figure 1e we show a transmission electron microscope (TEM) selected area electron diffraction (SAED) pattern measured on a QC-TBG suspended over a 2.5 μm diameter hole in a Si_3N_4 membrane, obtained via the same transfer method described above. The diffraction pattern consists of two sets of the monolayer graphene Bragg peaks, rotated at 30° relative to one another, resulting from the two (top and bottom) layers. The rotation angle is measured to be within 0.1° of 30°,

https://dx.doi.org/10.1021/acs.nanolett.0c00172
Nano Lett. 2020, 20, 3313−3319

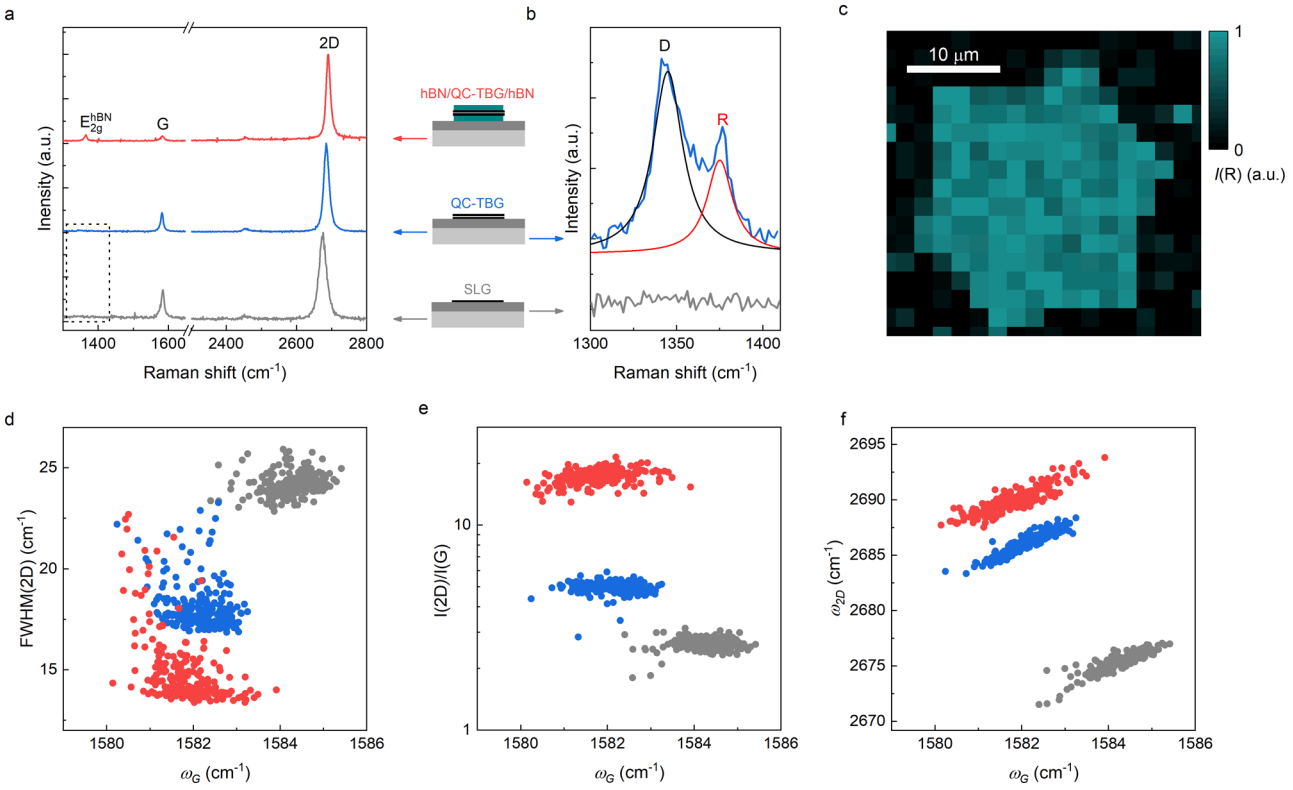

Figure 2. (a) Representative Raman spectra of SLG on SiO_2/Si (gray), QC-TBG on SiO_2/Si (blue), and hBN-encapsulated QC-TBG (red). All the samples are CVD grown on Cu and then transferred (and assembled) as described in the text. The sketches on the right-hand side identify the three structures considered (light gray = Si; dark gray = SiO_2; black = graphene; dark cyan = hBN). (b) Enlarged view of the low-energy region for SLG and QC-TBG on SiO_2/Si; the acquisition time was increased by ×20 with respect to the spectra in (a). The black and red lines are Lorentzian fits to the D and R modes of QC-TBG. (c) Scanning Raman mapping of the intensity of the R mode over the TBG area of the sample in Figure 1(d). (d–f) Correlation plots of fwhm(2D), $I(2D)/I(G)$, and ω_{2D} as a function of ω_G from 15 × 15 μm^2 areas of SLG on SiO_2/Si (gray), QC-TBG on SiO_2/Si (blue), and hBN-encapsulated QC-TBG (red). Each point corresponds to a single spectrum, acquired at a 1 μm interval.

given the uncertainty of the measurement (see Figure S3 for details). Likely more robust against slight image distortions, we observe 12-fold rotational symmetry in the fact that the $11\bar{2}0$ Bragg peaks from each layer are radially aligned with the $10\bar{1}0$ and $20\bar{2}0$ peaks from the other layer. This result was confirmed over numerous suspended QC-TBG regions (see Figure S3), proving high uniformity in the twist angle over distances of few tens of microns. In addition, in Figure S4, we present SAED on hBN-encapsulated QC-TBG, which confirms that the system maintains the growth-determined 12-fold rotational symmetry and interlayer rotation (within 0.2° of 30°) when subjected to van der Waals assembly. These observations identify our CVD graphene bilayers as dodecagonal quasicrystals and open the possibility of more in-depth studies of the electronic response of this system.

With this important piece of information in hand, we moved to a characterization of the QC-TBG with Raman spectroscopy (see SI for technical details). In Figure 2a, we compare representative Raman spectra of CVD grown SLG, QC-TBG, and hBN-encapsulated QC-TBG, all of them placed on SiO_2/Si. While AB bilayer graphene has a clear Raman fingerprint in the form of a multi-Lorentzian 2D peak[25] (see Figure S1), large-angle TBG provides the same Raman response as SLG, that is, sharp G and 2D peaks, although with minor rotation-dependent evolution and features.[26−29] In our QC-TBG samples, we could resolve a double peak structure in the low-energy 1300−1400 cm^{-1} region, which is completely absent for the surrounding SLG portions, as shown in Figure 2b. While for SLG this range is occupied by the defect-induced D band[25] (although absent in our SLG, indicating a negligible defect concentration), large-angle TBG is known to exhibit a D-like band[29] accompanied by an intervalley double-resonance R mode induced by the potential mutually imposed by the two layers.[26] In Figure 2c, we present a scanning Raman map of the intensity of the R mode over the TBG region of the sample shown in Figure 1d, which serves as a high-contrast alternative imaging approach for the QC-TBG. The R peak here is positioned at 1374(±6) cm^{-1}, in good accordance with the recent findings by Yao et al.,[9] who identified it as due to scattering with a reciprocal lattice vector of the second layer, a process specific to QC-TBG. As for the hBN-encapsulated QC-TBG, this peak could not be identified, due to its overlap with the high-intensity E_{2g} mode from the thick hBN crystals.

In Figure 2d–f, we present comparative correlation plots of the full width at half-maximum of the 2D peak fwhm(2D), intensity ratio of the 2D and G peaks $I(2D)/I(G)$, and frequency of the 2D peak ω_{2D}, respectively, as a function of the frequency of the G peak ω_G. The evolution of these characteristics from SLG to QC-TBG (gray to blue points) qualitatively matches the early report of Kim et al. for large-angle TBG:[27] fwhm(2D) drastically decreases, reaching values typically observed in hBN-encapsulated SLG;[30] $I(2D)/I(G)$ doubles, accompanied by a redshift of ω_G, indicating a reduction in the doping level,[31] which we ascribe to charge redistribution among the two graphene layers; and ω_{2D} blueshifts by 10 cm^{-1}, possibly due to a reduction of the global strain,[32] modification of the dielectric

https://dx.doi.org/10.1021/acs.nanolett.0c00172
Nano Lett. 2020, 20, 3313−3319

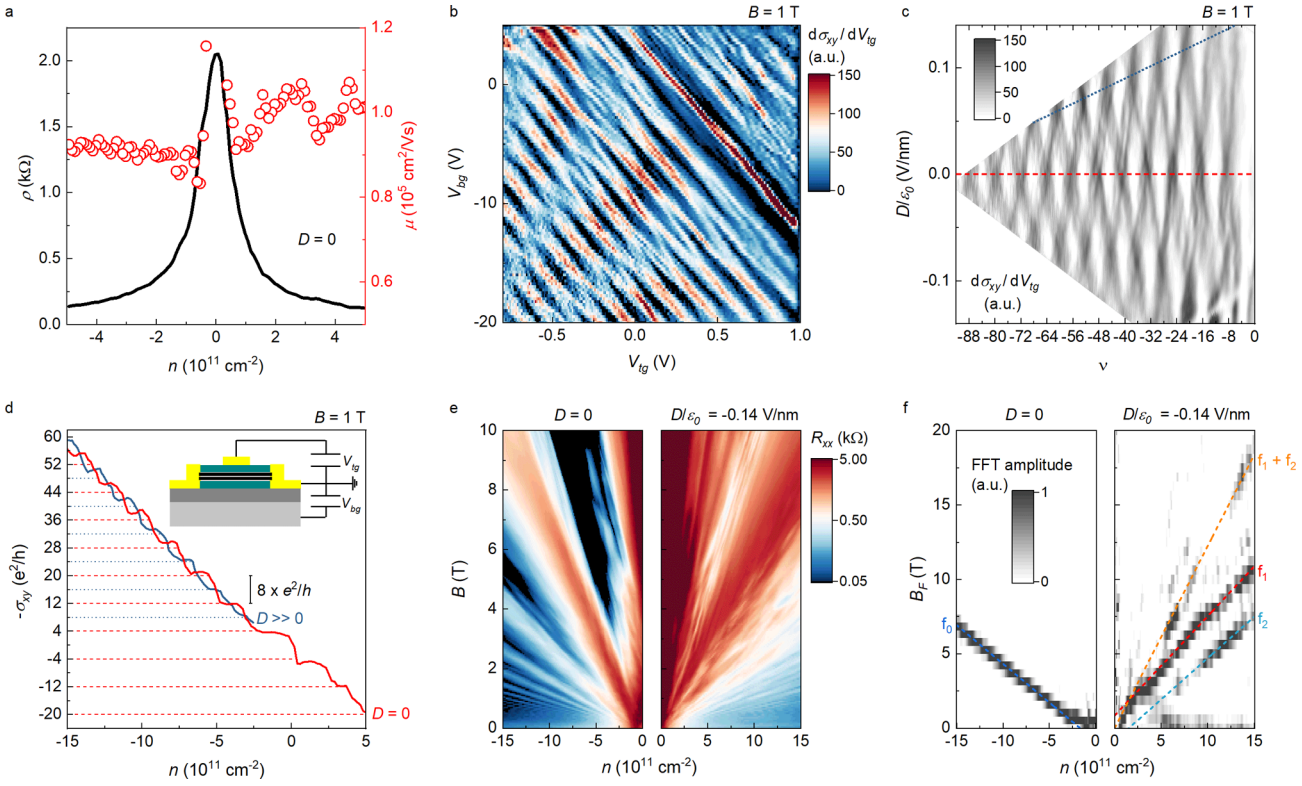

Figure 3. (a) Resistivity (black line) and carrier mobility (red circles) of sample D1 as a function of carrier density, at zero displacement field. (b) First derivative of σ_{xy} as a function of V_{tg} and V_{bg}, at $B = 1$ T. (c) Same data of (b) as a function of ν and D/ε_0. The red dashed line marks $D = 0$. The large D data in the following panel are taken along the blue dotted line. (d) Hall conductivity as a function of carrier density at $B = 1$ T, for $D = 0$ (red line) and $D \gg 0$ (blue line). The inset shows a schematic cross section of the devices studied (light gray = Si; dark gray = SiO_2; black = graphene; dark cyan = hBN; yellow = Cr/Au). (e) Longitudinal resistance as a function of carrier density for zero (left panel) and finite (right) displacement field. (f) FFT of the oscillatory component of the resistance data in (e). The dashed lines $f_{0,1,2}$ are fits the main peaks in the FFT spectra as a function of n, while $f_1 + f_2$ is the sum of the fits to the two splitted components. All of the data were acquired at $T = 4.2$ K.

environment,[33] or reduction of the Fermi velocity.[34] Upon dry encapsulation of QC-TBG in hBN (blue to red points), we found that fwhm(2D) is reduced to as low as 13 cm^{-1}, which is, to the best of our knowledge, the lowest value reported for hBN-encapsulated graphene, suggesting a drastic reduction of strain fluctuations and possibly a high-mobility electronic system. Moreover, the large increase of $I(2D)/I(G)$ indicates low doping and therefore the possibility of probing this system in the vicinity of the Dirac crossings. The further blueshift of ω_{2D}, finally, matches the findings of ref 33 regarding dielectric screening from hBN.

Starting from our hBN-encapsulated QC-TBG, we fabricated edge-contacted double-gated Hall bar devices for magnetotransport measurements (see sketch in Figure 3d inset and Figure S5). Figure 3 summarizes the main findings for high mobility device D1, while analogous results from the lower mobility device D2 are presented in Figure S6. In Figure 3a, we show the resistivity of D1 as a function of the carrier density n (black curve), measured at $T = 4.2$ K. By combining the top and bottom gate potentials V_{tg} and V_{bg}, we can modulate n while keeping the interlayer displacement field D fixed (in this case to $D = 0$, meaning an equal charge distribution between the two layers). In a double-gate configuration, $n = 1/e(C_{tg}V_{tg} + C_{bg}V_{bg}) - n_0$ and $D = (C_{tg}V_{tg} - C_{bg}V_{bg})/2 - D_0$, where C_{tg} and C_{bg} are the capacitance per unit area of the top and bottom gate, while n_0 and D_0 are residual carrier density and displacement field at zero gate voltages.[6] From gate-dependent Hall effect measurements of D1, we estimate $C_{tg} = 1.76 \times 10^{-7}$ F/cm^2, $C_{bg} = 1.05 \times 10^{-8}$ F/cm^2, and $n_0 = 2.6 \times 10^{11}$ cm^{-2}, while $D_0/\varepsilon_0 = 0.047$ V/nm is obtained by inspecting the resistivity oscillations. The narrow resistivity peak ($n^* = 3 \times 10^{10}$ cm^{-2}) and carrier mobility of 10^5 $cm^2/(V\ s)$ (red circles) are comparable to state-of-the-art devices based on CVD graphene,[14,15] assuring a low-disorder platform where the intrinsic electronic properties of the dodecagonal quasicrystal can be accessed. In Figure 3b, we show a map of the first derivative of the Hall conductivity $d\sigma_{xy}/dV_{tg}$ as a function of the two gate potentials, taken at fixed $B = 1$ T applied perpendicular to the device plane. Already at this moderate field, we can fully resolve an intricate pattern, with zeroes in $d\sigma_{xy}/dV_{tg}$ (black areas) corresponding to quantum Hall states, separated by a number of crossings between Landau levels (LLs). In Figure 3c we plot the same data as a function of the filling factor $\nu = 1/B \times h/e \times n$ and D/ε_0, where n and D are obtained via the relations specified above. Aligned along $D = 0$ (red dashed line), we observe a series of nodes separating quantum Hall states positioned at $\nu = -4, -12, -20, ...$, while at higher displacement field (blue dotted line) additional states arise at $\nu = -8, -16, -24, ...$ According to Sanchez-Yamagishi et al.,[6] this phenomenology is understood in terms of crossings between LLs belonging to independent graphene layers, controlled by modulation of n and D via the two gates. Across this pattern, the Hall conductivity σ_{xy} is expected to vary in the form of quantized steps $N \times e^2/h$, with N corresponding to the degeneracy of the LLs. In Figure 3d, we show σ_{xy} as a function of n for $D = 0$ (red line), and $D \gg 0$ (blue line, taken along the blue dotted line in Figure 3c), demonstrating two series of equally

https://dx.doi.org/10.1021/acs.nanolett.0c00172
Nano Lett. 2020, 20, 3313−3319

spaced plateaus at −4, −12, −20, ... × e^2/h and −8, −16, −24, ... × e^2/h, respectively. The degeneracy $N = 8$ is due to spin, valley, and layer degree of freedom, as in the case of two in-parallel uncoupled SLG.[6] If Dirac cones replica contributed to the density of states in QC-TBG, one would expect N in excess of 8. However, our data indicate the absence of additional degeneracies, ruling out this scenario. In addition, strong interlayer coupling should lead to anomalous screening properties of QC-TBG with respect to the independent SLG case.[8] We can directly probe the response of the system to field-effect doping by inspecting the positioning of the LLs crossing as a function of D (see Figure S7). Each crossing corresponds to a known difference in charge density and electrostatic potential between the two graphene sheets, from which we estimate an interlayer capacitance per unit area $C_{gg} = 6.9 \pm 1.4\ \mu F/cm^2$, in agreement with the reports of refs 6 and 35. When measuring a reference device, D3, made by artificial stacking of 30.2°-misaligned mechanically exfoliated graphene flakes,[13] we found completely analogous results (see Figure S8), thus confirming the uncoupled layers scenario. We investigated further the Fermi surface of QC-TBG, by measuring the resistance of D1 as a function of B (up to 10 T) and n, both for null and finite D (Figure 3e, left and right panels, respectively). For $D = 0$, we observed a standard fan diagram, with the oscillatory component of the resistance at fixed n showing a single frequency f_0 as a function of B^{-1}, as demonstrated by the fast Fourier transform spectra (FFT, see Figure 3f, left). We found that f_0 varies as a function of $|n|$ with slope $h/e \times 1/8$ (dashed blue line), which indicates a single 8-fold degenerate Fermi surface.[36] Applying a displacement field $D/\varepsilon_0 = -0.14$ V/nm (Figure 3e, right) is sufficient to lift the layers' degeneracy, resulting in a rather complex fan with numerous level crossings as a function of B and n. The corresponding FFT spectral map (Figure 3f, right) shows multiple peaks, with the two main frequencies f_1 and f_2 resulting from two layer-resolved Fermi surfaces, and the sum frequency $f_1 + f_2$ showing approximately double slope as compared to f_0, as expected for 4-fold degeneracy. On this basis, and with analogous data obtained on device D2, we can confirm that no Fermi contours, other than the ones surrounding the **K** and **K′** points of the two layers, contribute to the magnetotransport of QC-TBG.

Since the incommensurate dodecagonal quasicrystal emerges only at exact 30° rotation, it is important to discuss how variations in the twist angle within our experimental uncertainty (see Figures S3 and S4) can affect the electrical transport properties. So-called approximants of QC-TBG, that is, TBG with translational symmetry obtained by slight angular deviations from 30°[11] or changes in the lattice constant of one of the two layers,[12] show a smooth evolution of the density of states as a function of angle[11] and can accurately describe the photoemission results.[12] Based on those calculations, one expects the transport properties to be robust within tenths-of-degree variations (comparable to our experimental uncertainty) and, therefore, to be representative of QC-TBG ones. Extrinsic scattering of the charge carriers might also hinder the observation of anomalous interlayer coupling via electrical transport. Sample D1, however, shows very high carrier mobility at low temperature, ensuring a mean-free path in the order of the channel width (1 μm). While D2 surely incorporates more disorder, the results on the two devices do not differ significantly (e.g., one just needs to apply different magnitudes of magnetic and electric fields to resolve equivalent LLs patterns). In comparison to our hBN-encapsulated samples, which show minimal residual doping, the ones used in ref 8 present considerable coupling to the growth substrate. This is evidenced by a Fermi level of 0.3 eV for both graphene layers and a layer-asymmetric charge-transfer dynamic.[37] A possibility is that some of the ARPES results are specific to the SiC-supported system and/or to the highly doped regime. In this sense, we note that the samples of ref 9 are less doped and the authors report much weaker and limited-in-number Dirac cones replica. Nevertheless, in our experiments, we did not observe any anomaly as a function of field-effect doping up to 0.17 eV (corresponding to the largest carrier density measured in D2 at $D = 0$, calculated taking into account the layer degeneracy). Finally, one should consider the possibility that the extra Dirac cones are so-called final states, that is, purely spectroscopic features due to scattering of electrons at the surface *after* the photo excitation. Such elements, known both for single-layer graphene on SiC[38] and aligned graphene/hBN,[39] do not correspond to additional superpotential-induced states and, therefore, are not involved in the electrical transport: Under this scenario, our results are consistent and complementary to those of refs 8 and 9.

In conclusion, we show that large-area graphene bilayers with 30° interlayer rotation can be grown by CVD on Cu. This approach has several advantages, in particular, allowing for integration of the QC-TBG into hBN-encapsulated structures. Despite the PMMA-mediated transfer process, these samples exhibit extremely low doping and strain fluctuations, as shown by a Raman 2D peak as narrow as 13 cm^{-1}. The quantum Hall regime, fully developed at $B \leq 1$ T, presents gate-tunable 8-fold degenerate states, as for the standard case of uncoupled graphene layers. While QC-TBG probed by ARPES can show Dirac cones' replica with dodecagonal symmetry,[8] we have demonstrated that the low-energy band structure and density of states—the physical properties probed by magnetotransport—are unaffected by this mechanism. During the review process, we became aware that Deng et al.[40] have come to similar conclusions via scanning tunneling spectroscopy of QC-TBG near the Dirac point. Theoretical calculations, however, suggest important modifications due to interlayer coupling when populating the bands up to few eV,[11,12] a regime not accessible with standard field-effect devices, calling for alternative experimental techniques. In more general terms, our work demonstrates an alternative approach to high-quality electrical transport experiments in twisted graphene layers, where the twist angle is precisely determined during rapid CVD growth of a macroscopic number of large-area samples, without imposing limitations in terms of carrier mobility. While at present the twist angle cannot be arbitrarily selected such as in the tear-and-stack approach, advancements in the control of the Cu surface morphology might enable to obtain arbitrary and controlled deviations from both the AB and 30°-rotated stacking orders.

■ ASSOCIATED CONTENT

Supporting Information

The Supporting Information is available free of charge at https://pubs.acs.org/doi/10.1021/acs.nanolett.0c00172.

Details on the experimental methods for CVD growth, semi-dry transfer from Cu to SiO_2/Si, encapsulation in hBN, TEM, Raman spectroscopy, device fabrication, and low-temperature magnetotransport. Figures S1−S8 (PDF)

https://dx.doi.org/10.1021/acs.nanolett.0c00172
Nano Lett. 2020, 20, 3313−3319

AUTHOR INFORMATION

Corresponding Authors

Sergio Pezzini − *Center for Nanotechnology Innovation @NEST and Graphene Labs, Istituto Italiano di Tecnologia, 56127 Pisa, Italy;* orcid.org/0000-0003-4289-907X; Email: sergio.pezzini@iit.it

Camilla Coletti − *Center for Nanotechnology Innovation @NEST and Graphene Labs, Istituto Italiano di Tecnologia, 56127 Pisa, Italy;* orcid.org/0000-0002-8134-7633; Email: camilla.coletti@iit.it

Authors

Vaidotas Mišeikis − *Center for Nanotechnology Innovation @NEST and Graphene Labs, Istituto Italiano di Tecnologia, 56127 Pisa, Italy*

Giulia Piccinini − *Center for Nanotechnology Innovation @NEST, Istituto Italiano di Tecnologia, 56127 Pisa, Italy; NEST, Scuola Normale Superiore, 56127 Pisa, Italy*

Stiven Forti − *Center for Nanotechnology Innovation @NEST, Istituto Italiano di Tecnologia, 56127 Pisa, Italy*

Simona Pace − *Center for Nanotechnology Innovation @NEST and Graphene Labs, Istituto Italiano di Tecnologia, 56127 Pisa, Italy*

Rebecca Engelke − *Department of Physics, Harvard University, Cambridge, Massachusetts 02138, United States*

Francesco Rossella − *NEST, Scuola Normale Superiore, 56127 Pisa, Italy; NEST, Istituto Nanoscienze-CNR, 56127 Pisa, Italy;* orcid.org/0000-0002-0601-4927

Kenji Watanabe − *National Institute for Materials Science, Tsukuba 305-0044, Japan;* orcid.org/0000-0003-3701-8119

Takashi Taniguchi − *National Institute for Materials Science, Tsukuba 305-0044, Japan;* orcid.org/0000-0002-1467-3105

Philip Kim − *Department of Physics, Harvard University, Cambridge, Massachusetts 02138, United States;* orcid.org/0000-0002-8255-0086

Complete contact information is available at: https://pubs.acs.org/10.1021/acs.nanolett.0c00172

Notes

The authors declare no competing financial interest.

ACKNOWLEDGMENTS

The authors thank Pilkyung Moon and Vladimir Fal'ko for useful discussions. Growth of hexagonal boron nitride crystals was supported by the Elemental Strategy Initiative conducted by the MEXT, Japan and the CREST(JPMJCR15F3), JST. The research leading to these results has received funding from the European Union's Horizon 2020 research and innovation program under grant agreement no. 785219-GrapheneCore2 and 881603-GrapheneCore3. The work at Harvard is supported by ONR (N00014-15-1-2761).

REFERENCES

(1) Cao, Y.; Fatemi, V.; Demir, A.; Fang, S.; Tomarken, S. L.; Luo, J. Y.; Sanchez-Yamagishi, J. D.; Watanabe, K.; Taniguchi, T.; Kaxiras, E.; Ashoori, R. C.; Jarillo-Herrero, P. Correlated insulator behaviour at half-filling in magic-angle graphene superlattices. *Nature* **2018**, *556*, 80−84.

(2) Cao, Y.; Fatemi, V.; Fang, S.; Watanabe, K.; Taniguchi, T.; Kaxiras, E.; Jarillo-Herrero, P. Unconventional superconductivity in magic-angle graphene superlattices. *Nature* **2018**, *556*, 43−50.

(3) Li, G.; Luican, A.; Lopes dos Santos, J. M. B.; Castro Neto, A. H.; Reina, A.; Kong, J.; Andrei, E. Y. Observation of Van Hove singularities in twisted graphene layers. *Nat. Phys.* **2010**, *6*, 109−113.

(4) Luican, A.; Li, G.; Reina, A.; Kong, J.; Nair, R. R.; Novoselov, K. S.; Geim, A. K.; Andrei, E. Y. Single-layer behavior and its breakdown in twisted graphene layers. *Phys. Rev. Lett.* **2011**, *106*, 126802.

(5) Wong, D.; Wang, Y.; Jung, J.; Pezzini, S.; DaSilva, A. M.; Tsai, H.-Z.; Jung, H. S.; Khajeh, R.; Kim, Y.; Lee, J.; Kahn, S.; Tollabimazraehno, S.; Rasool, H.; Watanabe, K.; Taniguchi, T.; Zettl, A.; Adam, S.; MacDonald, A. H.; Crommie, M. F. Local spectroscopy of moiré-induced electronic structure in gate-tunable twisted bilayer graphene. *Phys. Rev. B: Condens. Matter Mater. Phys.* **2015**, *92*, 155409.

(6) Sanchez-Yamagishi, J. D.; Taychatanapat, T.; Watanabe, K.; Taniguchi, T.; Yacoby, A.; Jarillo-Herrero, P. Quantum Hall effect, screening, and layer-polarized insulating states in twisted bilayer graphene. *Phys. Rev. Lett.* **2012**, *108*, 076601.

(7) Sanchez-Yamagishi, J. D.; Luo, J. Y.; Young, A. F.; Hunt, B.; Watanabe, K.; Taniguchi, T.; Ashoori, R. C.; Jarillo-Herrero, P. Helical edge states and fractional quantum Hall effect in a graphene electron−hole bilayer. *Nat. Nanotechnol.* **2017**, *12*, 118−122.

(8) Ahn, S. J.; Moon, P.; Kim, T.-H.; Kim, H.-W.; Shin, H.-C.; Kim, E. H.; Cha, H. W.; Kahng, S.-J.; Kim, P.; Koshino, M.; Son, Y.-W.; Yang, C.-W.; Ahn, J. R. Dirac electrons in a dodecagonal graphene quasicrystal. *Science* **2018**, *361*, 782−786.

(9) Yao, W.; Wang, E.; Bao, C.; Zhang, Y.; Zhang, K.; Bao, K.; Chan, C. K.; Chen, C.; Avila, J.; Asensio, M. C.; Zhu, J.; Zhou, S. Quasicrystalline 30° twisted bilayer graphene as an incommensurate superlattice with strong interlayer coupling. *Proc. Natl. Acad. Sci. U. S. A.* **2018**, *115*, 6928−6933.

(10) Spurrier, S.; Cooper, N. R. Theory of quantum oscillations in quasicrystals: Quantizing spiral Fermi surfaces. *Phys. Rev. B: Condens. Matter Mater. Phys.* **2019**, *100*, No. 081405.

(11) Moon, P.; Koshino, M.; Son, Y.-W. Quasicrystalline electronic states in 30° rotated twisted bilayer graphene. *Phys. Rev. B: Condens. Matter Mater. Phys.* **2019**, *99*, 165430.

(12) Yu, G.; Wu, Z.; Zhan, Z.; Katsnelson, M. I.; Yuan, S. Dodecagonal bilayer graphene quasicrystal and its approximants. *npj Computational Materials* **2019**, *5*, 122.

(13) Kim, K.; Yankowitz, M.; Fallahazad, B.; Kang, S.; Movva, H. C. P.; Huang, S.; Larentis, S.; Corbet, C. M.; Taniguchi, T.; Watanabe, K.; Banerjee, S. K.; LeRoy, B. J.; Tutuc, E. van der Waals heterostructures with high accuracy rotational alignment. *Nano Lett.* **2016**, *16*, 1989−1995.

(14) Schmitz, M.; Engels, S.; Banszerus, L.; Watanabe, K.; Taniguchi, T.; Stampfer, C.; Beschoten, B. High mobility dry-transferred CVD bilayer graphene. *Appl. Phys. Lett.* **2017**, *110*, 263110.

(15) De Fazio, D.; Purdie, D. G.; Ott, A. K.; Braeuninger-Weimer, P.; Khodkov, T.; Goossens, S.; Taniguchi, T.; Watanabe, K.; Livreri, P.; Koppens, F. H. L.; Hofmann, S.; Goykhman, I.; Ferrari, A. C.; Lombardo, A. High-mobility, wet-transferred graphene grown by chemical vapor deposition. *ACS Nano* **2019**, *13*, 8926−8935.

(16) Yan, Z.; Liu, Y.; Ju, L.; Peng, Z.; Lin, J.; Wang, G.; Zhou, H.; Xiang, C.; Samuel, E. L. G.; Kittrell, C.; Artyukhov, V. I.; Wang, F.; Yakobson, B. I.; Tour, J. M. Large Hexagonal Bi-and Trilayer Graphene Single Crystals with Varied Interlayer Rotations. *Angew. Chem., Int. Ed.* **2014**, *53*, 1565−1569.

(17) Gao, Z.; Zhang, Q.; Naylor, C. H.; Kim, Y.; Abidi, I. H.; Ping, J.; Ducos, P.; Zauberman, J.; Zhao, M.-Q.; Rappe, A. M.; Luo, Z.; Ren, L.; Johnson, A. T. C. Crystalline bilayer graphene with preferential stacking from Ni−Cu gradient alloy. *ACS Nano* **2018**, *12*, 2275−2282.

(18) Miseikis, V.; Convertino, D.; Mishra, N.; Gemmi, M.; Mashoff, T.; Heun, S.; Haghighian, N.; Bisio, F.; Canepa, M.; Piazza, V.; Coletti, C. Rapid CVD growth of millimetre-sized single crystal graphene using a cold-wall reactor. *2D Mater.* **2015**, *2*, 014006.

(19) Miseikis, V.; Bianco, F.; David, J.; Gemmi, M.; Pellegrini, V.; Romagnoli, M.; Coletti, C. Deterministic patterned growth of high-mobility large-crystal graphene: a path towards wafer scale integration. *2D Mater.* **2017**, *4*, 021004.

(20) Shibuta, Y.; Elliott, J. A. Interaction between two graphene sheets with a turbostratic orientational relationship. *Chem. Phys. Lett.* **2011**, *512*, 146−150.
(21) Wang, Y.; Zheng, Y.; Xu, X.; Dubuisson, E.; Bao, Q.; Lu, J.; Loh, K. P. Electrochemical Delamination of CVD-Grown Graphene Film: Toward the Recyclable Use of Copper Catalyst. *ACS Nano* **2011**, *5*, 9927−9933.
(22) Purdie, D. G.; Pugno, N. M.; Taniguchi, T.; Watanabe, K.; Ferrari, A. C.; Lombardo, A. Cleaning interfaces in layered materials heterostructures. *Nat. Commun.* **2018**, *9*, 5387.
(23) Wang, L.; Gao, Y.; Wen, B.; Han, Z.; Taniguchi, T.; Watanabe, K.; Koshino, M.; Hone, J.; Dean, C. R. Evidence for a fractional fractal quantum Hall effect in graphene superlattices. *Science* **2015**, *350*, 1231−1234.
(24) Zhu, M.; Ghazaryan, D.; Son, S.-K.; Woods, C. R.; Misra, A.; He, L.; Taniguchi, T.; Watanabe, K.; Novoselov, K. S.; Cao, Y.; Mishchenko, A. Stacking transition in bilayer graphene caused by thermally activated rotation. *2D Mater.* **2017**, *4*, 011013.
(25) Ferrari, A. C.; Meyer, J. C.; Scardaci, V.; Casiraghi, C.; Lazzeri, M.; Mauri, F.; Piscanec, S.; Jiang, D.; Novoselov, K. S.; Roth, S.; Geim, A. K. Raman Spectrum of Graphene and Graphene Layers. *Phys. Rev. Lett.* **2006**, *97*, 187401.
(26) Carozo, V.; Almeida, C. M.; Ferreira, E. H. M.; Cancado, L. G.; Achete, C. A.; Jorio, A. Raman Signature of Graphene Superlattices. *Nano Lett.* **2011**, *11*, 4527−4534.
(27) Kim, K.; Coh, S.; Tan, L. Z.; Regan, W.; Yuk, J. M.; Chatterjee, E.; Crommie, M. F.; Cohen, M. L.; Louie, S. G.; Zettl, A. Raman Spectroscopy Study of Rotated Double-Layer Graphene: Misorientation-Angle Dependence of Electronic Structure. *Phys. Rev. Lett.* **2012**, *108*, 246103.
(28) He, R.; Chung, T.-F.; Delaney, C.; Keiser, C.; Jauregui, L. A.; Shand, P. M.; Chancey, C. C.; Wang, Y.; Bao, J.; Chen, Y. P. Observation of Low Energy Raman Modes in Twisted Bilayer Graphene. *Nano Lett.* **2013**, *13*, 3594−3601.
(29) Carozo, V.; Almeida, C. M.; Fragneaud, B.; Bedê, P. M.; Moutinho, M. V. O.; Ribeiro-Soares, J.; Andrade, N. F.; Souza Filho, A. G.; Matos, M. J. S.; Wang, B.; Terrones, M.; Capaz, R. B.; Jorio, A.; Achete, C. A.; Cançado, L. G. Resonance effects on the Raman spectra of graphene superlattices. *Phys. Rev. B: Condens. Matter Mater. Phys.* **2013**, *88*, 085401.
(30) Neumann, C.; Reichardt, S.; Venezuela, P.; Drögeler, M.; Banszerus, L.; Schmitz, M.; Watanabe, K.; Taniguchi, T.; Mauri, F.; Beschoten, B.; Rotkin, S. V.; Stampfer, C. Raman spectroscopy as probe of nanometre-scale strain variations in graphene. *Nat. Commun.* **2015**, *6*, 8429.
(31) Das, A.; Pisana, S.; Chakraborty, B.; Piscanec, S.; Saha, S. K.; Waghmare, U. V.; Novoselov, K. S.; Krishnamurthy, H. R.; Geim, A. K.; Ferrari, A. C.; Sood, A. K. Monitoring dopants by Raman scattering in an electrochemically top-gated graphene transistor. *Nat. Nanotechnol.* **2008**, *3*, 210−215.
(32) Lee, J. E.; Ahn, G.; Shim, J.; Lee, Y. S.; Ryu, S. Optical separation of mechanical strain from charge doping in graphene. *Nat. Commun.* **2012**, *3*, 1024.
(33) Forster, F.; Molina-Sanchez, A.; Engels, S.; Epping, A.; Watanabe, K.; Taniguchi, T.; Wirtz, L.; Stampfer, C. Dielectric screening of the Kohn anomaly of graphene on hexagonal boron nitride. *Phys. Rev. B: Condens. Matter Mater. Phys.* **2013**, *88*, 085419.
(34) Ni, Z.; Wang, Y.; Yu, T.; You, Y.; Shen, Z. Reduction of Fermi velocity in folded graphene observed by resonance Raman spectroscopy. *Phys. Rev. B: Condens. Matter Mater. Phys.* **2008**, *77*, 235403.
(35) Rickhaus, P.; Liu, M.-H.; Kurpas, M.; Kurzmann, A.; Lee, Y.; Overweg, H.; Eich, M.; Pisoni, R.; Taniguchi, T.; Watanabe, K.; Richter, K.; Ensslin, K.; Ihn, T. The electronic thickness of graphene. *Sci. Adv.* **2020**, *6*, eaay8409.
(36) Shoenberg, D. *Magnetic Oscillations in Metals*; Cambridge University Press: Cambridge, England, 1984.
(37) Suzuki, T.; Iimori, T.; Ahn, S. J.; Zhao, Y.; Watanabe, M.; Xu, J.; Fujisawa, M.; Kanai, T.; Ishii, N.; Itatani, J.; Suwa, K.; Fukidome, H.; Tanaka, S.; Ahn, J. R.; Okazaki, K.; Shin, S.; Komori, F.; Matsuda, I. Ultrafast Unbalanced Electron Distributions in Quasicrystalline 30° Twisted Bilayer Graphene. *ACS Nano* **2019**, *13*, 11981−11987.
(38) Bostwick, A.; Ohta, T.; McChesney, J. L; Emtsev, K. V; Seyller, T.; Horn, K.; Rotenberg, E. Symmetry breaking in few layer graphene films. *New J. Phys.* **2007**, *9*, 385.
(39) Mucha-Kruczyński, M.; Wallbank, J. R.; Fal'ko, V. I. Moiré miniband features in the angle-resolved photoemission spectra of graphene/hBN heterostructures. *Phys. Rev. B: Condens. Matter Mater. Phys.* **2016**, *93*, 085409.
(40) Deng, B.; Wang, B.; Li, N.; Li, R.; Wang, Y.; Tang, J.; Fu, Q.; Tian, Z.; Gao, P.; Xue, J.; Peng, H. Interlayer Decoupling in 30° Twisted Bilayer Graphene Quasicrystal. *ACS Nano* **2020**, *14*, 1656−1664.

https://dx.doi.org/10.1021/acs.nanolett.0c00172
Nano Lett. 2020, 20, 3313−3319